

Journal Article

**Explicit Finite Element Modelling as a Development Tool for New
Ultrasound Testing Methodologies for Detection and
Characterization of Porosity and Defects in Composites**

McMillan, A. J. and Holeczek, K.

This article is published by ASTM International. The definitive version of this article is available at:
http://www.astm.org/DIGITAL_LIBRARY/JOURNALS/MPC/PAGES/MPC20150047.htm

Recommended citation:

McMillan, A. J. and Holeczek, K. (2016), 'Explicit Finite Element Modelling as a Development Tool for New Ultrasound Testing Methodologies for Detection and Characterization of Porosity and Defects in Composites,' *Materials Performance and Characterization*, Vol. 5, No.1, pp. 78-98, doi: 10.1520/MPC20150047

Explicit Finite Element Modelling as a Development Tool for New Ultrasound Testing Methodologies for Detection and Characterization of Porosity and Defects in Composites

AUTHORS: AJ McMillan¹, K Holeczek²

ABSTRACT: Composite components frequently contain porosity or defects, which might, in some circumstances, be deemed benign. Other defects could lead to progressive or sudden failure in service, hence reliable and accurate material condition monitoring and health assessment is an important prerequisite for further design for the use of composite materials in high duty and life sensitive engineering components. The objective of this paper is to demonstrate the use of explicit finite element as an effective development tool in the development of ultrasound testing methodologies for the characterization of porosity in composites – a virtual ultrasound vibration laboratory. This would enable an improved inspection sentencing capability for as-manufactured composite structural components. It would also be of benefit in sentencing components subject to foreign object damage (FOD), in order to determine whether the component can continue in service, possibly with in-service monitoring or cosmetic repair, or must be condemned. In this work, finite element models simulating damage and porosity are presented. The models are compared with ultrasound tests on real specimens with practically relevant defects. Experimental tests, making use of wave superposition from two piezo-electric vibration sources, are shown to detect energy absorbing damage in the specimen, such as might have been created by impact or crush loads. The same piezo-electric vibration system is also used to measure the dissipated energy. Computational analysis, using simple material model variations, is able to replicate the Lamb wave generation and evolve a wave form resembling a “standing wave”. The computational material model is modified to represent porosity in composites.

KEYWORDS: structural health monitoring, explicit finite element, composites, solid wave interferences, porosity detection

1. Introduction

The design of critical, high duty or dynamically-loaded aerospace structures, *e.g.* the fuselage and wings of an aircraft or the airfoils and structures of the engine, is characterized by the trade-off between performance and weight [1]. High failure-tolerance, especially in consideration of unpredictable events such as bird impact, poses additional design

¹ a.mcmillan@glyndwr.ac.uk, Glyndwr University, Computational Mechanics, Manufacturing simulation, Design and Optimisation (CoMManDO) Research Group, Applied Science, Computing and Engineering Division, Mold Road, Wrexham, LL11 2AW, UK. orcid.org/0000-0003-4191-096X.

² klaudiusz.holeczek@tu-dresden.de, Technische Universität Dresden, Institute of Lightweight Engineering and Polymer Technology (ILK), Holbeinstr. 3, 01307, Dresden, Germany. orcid.org/0000-0002-2177-0448.

objectives [2–5]. Modern fiber reinforced composite materials, with good damage tolerance properties, high specific anisotropic stiffness and high strength, are particularly suitable for such high-performance applications [6].

In the engineering design of high duty components, specified requirements for strength and component life must be met. In the development of a component lifing strategy, inspection service intervals and non-destructive evaluation (NDE) methods are prescribed. Depending on the choice of lifing strategy, it might be deemed acceptable for some damage initiation and growth to take place, but the extent of such damage must be measurable, and the growth rate predictable. Reliable and accurate material condition monitoring and health assessment is therefore an important prerequisite for damage tolerant design. In-service inspection of the structural condition of a component will typically comprise optical examination, or ultrasonic investigation. More expensive and labor-intensive NDE techniques such as computed tomography analysis, or inspections that require significant disassembly are undesirable because they significantly impact on the operation time of the machine under inspection. A shift of strategy towards condition-based inspection can significantly reduce maintenance costs and improve reliability through timely introduction of appropriate measures [7].

Recent progress in the fields of sensor technology, composite manufacturing processes, signal analysis, and computational intelligence has stimulated the development of material-integrated structural health monitoring systems. A common requirement of such systems is the application of measurable, damage-sensitive physical quantities for detection, localization, and quantification of faults [8–12]. The damping performance of anisotropic material has been identified as such a sensitive physical quantity, and this is especially the case concerning composite materials subject to different damage types [13; 14]. The development of a measurement methodology exploiting this could lead to broader application in both NDE and structural health monitoring.

Current typical non-destructive experimental methods for the determination of the material damping, *e.g.* relaxation, forced and free-vibration or thermal energy balance tests, have limited spatial resolution [15], and therefore do not allow a reliable measurement of material damping property variation in a localized region, such as one affected by a low-energy impact. This paper builds on the application of a method [16] which has demonstrated the potential for the detection of localized material damage or porosity based on the material damping changes.

In the current paper, explicit finite element method has been used as an effective development tool. Explicit finite element analysis has long been used for modelling impact and crash, and the models developed in the aerospace and automotive industries run to tens of millions of elements. Thus for a small component, it is perfectly feasible to develop a finite element model for which the mesh dimensions are smaller than a tenth of the wavelength of an ultrasound wave passing through that component. Such a model can be used as a virtual ultrasound vibration laboratory [17].

2. Description of the testing procedure

Phenomenological description of the method

The method is one of a number of related techniques that use mechanical wave properties for the determination of material parameters. The characteristic feature of this method is the application of a tuned localized “standing wave” used in combination with appropriate signal analysis algorithms. (This is not a true standing wave in the purest sense, but is created by the superposition of two travelling waves.) Such an approach enables the determination of the damping distribution along the path connecting the stationary wave sources [18].

Mechanical wave characteristics, such as amplitude or propagation velocity, depend on the mechanical properties of the medium in which the wave propagates: a change in the mechanical properties – material stiffness or damping – is reflected in a modification of the features of the wave. The particular mechanical wave used here, is a localized “standing wave”, generated by the interference of two mechanical waves with the same wavelengths and amplitudes travelling together from opposite directions.

In order to demonstrate the physical basis of the proposed concept, it is convenient to use a viscoelastic material model to represent the vibrational energy absorbing effects of practically occurring [19] damage-caused dry friction. Assuming the VOIGT material model, the mechanical work per cycle and per unit volume W , and hence the dissipated energy of a vibrating structure is [20]:

$$W = \frac{\mu'(\omega)}{\omega} \oint (\dot{\varepsilon}^*)^2 dt$$

where $\dot{\varepsilon}^*$ is the complex strain velocity; ω is the angular frequency; t is time; and μ' is the component of the complex second LAMÉ parameter representing viscous damping.

Assuming that μ' and $\dot{\varepsilon}^*$ are unevenly distributed, the dissipated mechanical work is not uniform in the analyzed volume. The term $\dot{\varepsilon}^*$ represents a weighting of the dissipated energy, assuming that the distribution of $\dot{\varepsilon}^*$ is independent of damping distribution.

The damping in the regions with the maximal “standing wave” velocities (anti-nodes) has the highest weighting, whereas the weighting for regions with zero oscillation deflection (nodes) is equal to zero. A shift of the node and anti-node position, by a modification of the phase of the travelling waves, causes a defined change of the weighting distribution applied to the analyzed regions. The localized damping distribution can be deduced through analysis of the work done by the actuators as a function of the phase of the travelling waves. This is described in detail by KOSTKA *et. al.* [16].

Preliminary experimental investigations

To make practical use of the method, it is necessary to be able to determine the dissipated mechanical energy experimentally, since the analysis of energy is the basis for the

identification of the localized damage regions. The dissipated energy can be estimated from the relation between the electro-mechanical admittance, \bar{Y}_E , of the piezoceramic-based actuator and the mechanical impedance of the structure to which the actuator is attached [21]:

$$\bar{Y}_E = \bar{Y}_P + \bar{Y}_A$$

where \bar{Y}_P depends solely on the parameters of the piezoceramic-based actuator, and is therefore a passive component since it is not affected by any damage to the structure. The second term, \bar{Y}_A , represents the coupled interaction between the structure and the piezoceramic-based actuator. The value of \bar{Y}_A changes as a result of a modification in the mechanical properties, *i.e.* as a result of damage. As a consequence, the electro-mechanical admittance of the piezoceramic-based actuator, \bar{Y}_E , is also altered.

While driving the piezoceramic-based actuator with a voltage, $V(t)$, the resulting electrical current, $I(t, \bar{Y}_E)$, is also changed, according to generalized OHM's law. The dissipated energy, (\bar{Y}_E) , can be calculated from the time series of voltage and current as an integral over one period:

$$W(\bar{Y}_E) = \oint U(t) I(t, \bar{Y}_E) dt$$

Investigated structure

The structure used in the experiments was a laminated beam of length 700 mm, breadth 30 mm, and thickness 4.2 mm, made of 32 layer flat-bed weft-knitted glass fiber reinforced polypropylen, in a layup defined by $[0/90_2/0]_{4s}$. Circular piezoelectric transducers with a diameter of 10 mm and height 0.3 mm were applied to the surface of the beam using epoxy-based adhesive, Fig. 1. Glass beads with a diameter of 15 μm were admixed to the adhesive to guarantee a defined thickness.

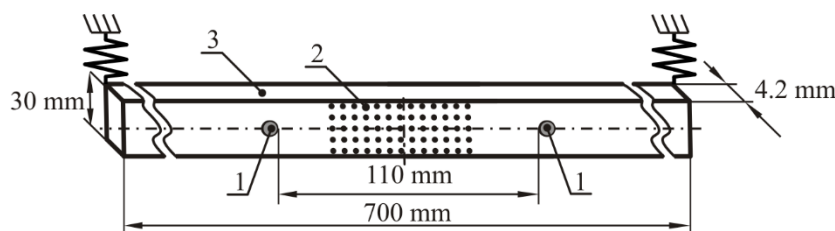


Figure 1: Geometrical configuration of the investigated structure. 1 – piezoceramic-based actuator, 2 – gauge section containing measuring points for the laser scanning vibrometer, 3 – investigated beam structure

The piezoceramic-based actuators (Produced by PI CERAMICS GMBH, Material PIC 255 with Ag electrodes) were driven by a HANN windowed tone burst sinusoidal signal of fundamental

frequency 7812.5 Hz and three periods duration. The windowing was applied to minimize unwanted dispersion effects [22]. The generated within MATLAB programming environment signals were send via the multifunction data acquisition analog-digital card NI PCI-6259 to a voltage amplifier (Produced by TREK INC., Model PA05039).

In order to prove that a “standing wave” with variable position can be generated, the out-of-plane velocity within the gauged section between the transducers was recorded using a laser scanning vibrometer system (Produced by POLYTEC GMBH, Typ PSV-400, Single laser head). The results are presented in Fig. 2 are the averaged result from 100 measurements.

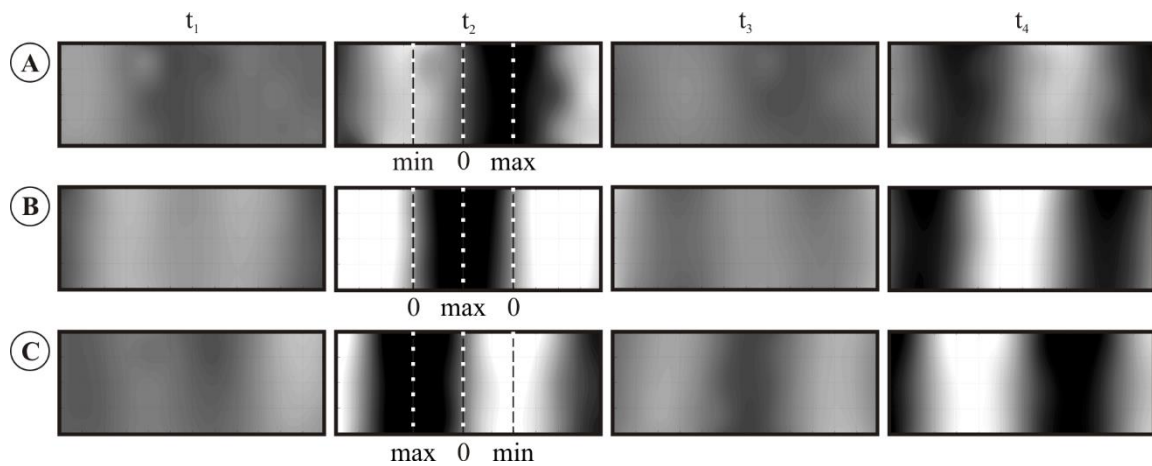


Figure 2: Time sequences of the experimentally determined out-of-plane velocities (time images are for $t_1 < t_2 < t_3 < t_4$).

(A) Initial phase of the travelling waves = $-\frac{\pi}{2}$

(B) Initial phase of the travelling waves = 0

(C) Initial phase of the travelling waves = $\frac{\pi}{2}$

The recorded time sequences confirm the formation of a “standing wave” for the selected excitation frequency. Since the wavelength was large in proportion to the width of the specimen, the wave can be considered as plane wave, and accordingly, the direction-dependent effects connected with anisotropy of mechanical properties can be neglected. By modifying the relative phase of the piezoceramic-based actuators the location of the “standing wave” could be shifted along the gauge section between the wave sources.

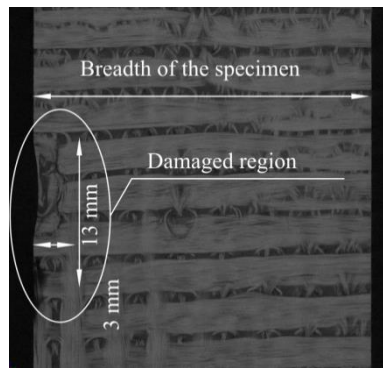


Figure 3: Computed tomography examination of the damaged specimen.

A reference state for a pristine specimen, comprising the time series for the electrical voltage and current, was stored for later analysis. Subsequently, a defined quantity of damage was introduced to the specimen using a 3-point bending test. The specimen was placed on two support rollers of radius of 10 mm and a distance of 70 mm apart, and loaded with a punch having the same radius at the center of the specimen. The punch was moved towards the specimen at a speed of 2 mm/min until the first visible signs of damage occurred, at a force of 3154.72 N. The damage position and extent was gauged using a computed tomography system (Produced by GE Measurement & Control, Type phoenix v|tome|x L 450 with unipolar minifocus X-ray tube, with spatial resolution $10\mu\text{m}$). The results confirmed that the damage had been successfully initiated, Fig. 3. The approximate size of the damaged area was found to be $3\text{ mm} \times 13\text{ mm}$, and it extended through the entire thickness. This information was later used for validation.

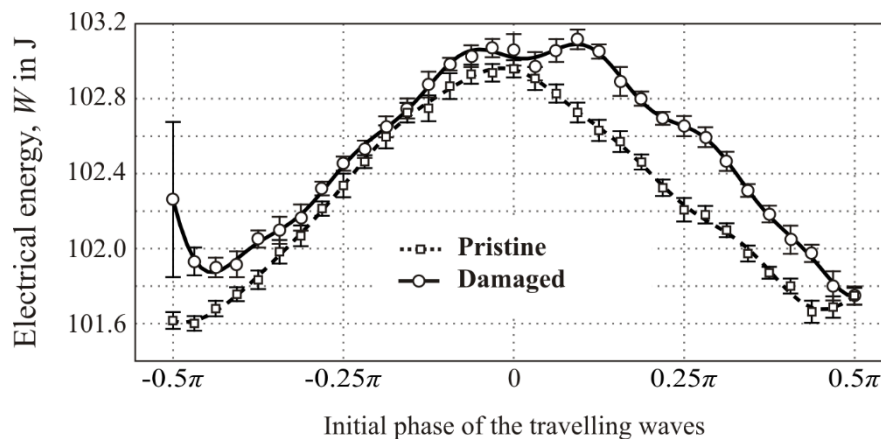


Figure 4: Experimentally determined dissipated energy for pristine and damaged specimens.

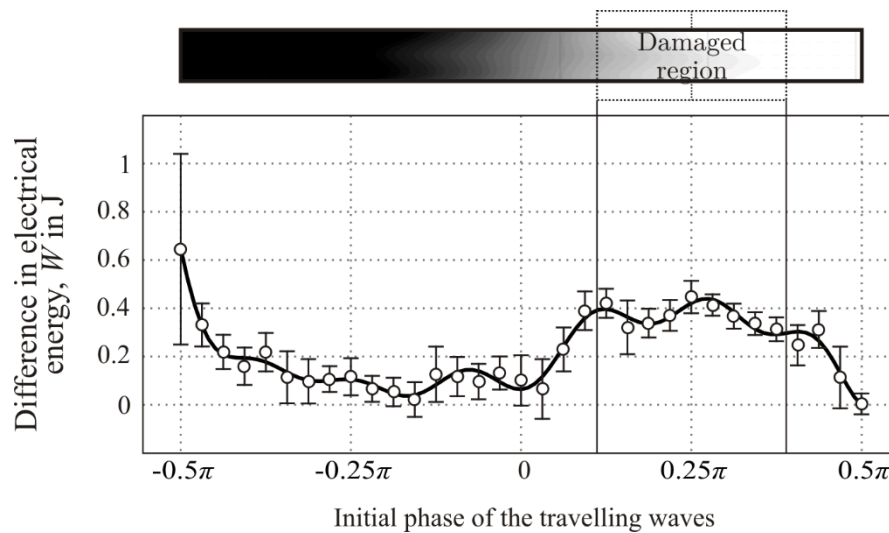


Figure 5: Identification of the damage region location from the difference in dissipated electrical energy between damaged and pristine specimens.

Figure 4 shows the electrical work done by the actuators, as a function of the relative phase of the vibration sources, for both the pristine and damaged specimens.

The rather high level of energy dissipated for the pristine specimen can be explained as a consequence of the viscoelastic properties the composite material under investigation. To account for this effect and to see only the energy dissipation arising from damage, the difference between the two signals is shown, Fig. 5.

The position of the maximum of the difference in dissipated energy is in correspondence with the position of the anti-node of the “standing wave” at the damaged region. It was possible to detect both the location and the extent of damaged region.

3. Computational Models

Geometrical considerations

The computational analysis model was built and run in Abaqus 6.14 / explicit, following observations from the experimental measurements, and with a view to representing all the most significant features. This geometry is shown in Fig. 6. The gauge section, length 110 mm, is the region between the two forcing pads. For convenience of modelling, this is divided into eleven regions of equal size: from left to right, Region 1L, Region 2L, Region 3L, Region 4L, Region 5L, Centre Region, Region 5R, Region 4R, Region 3R, Region 2R, and Region 1R. As in the experimental work, the objective of the analysis is to identify regions within the gauge section where material properties are modified (*i.e.* “damaged”) by interpreting the model vibration energy data.

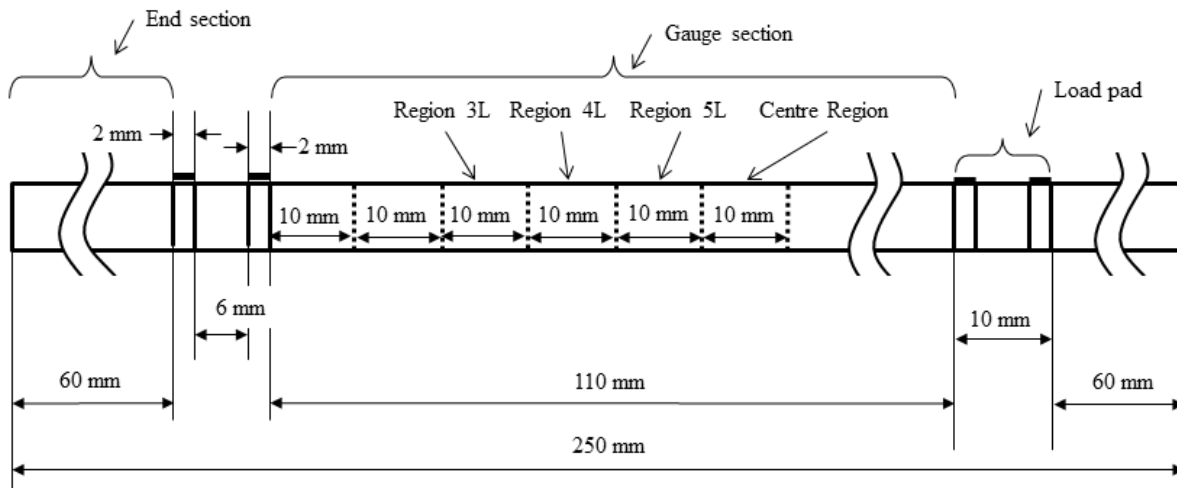


Figure 6: Schematic of the geometry of the analysis model (not to scale).

In view of the need to keep computational time manageable, the model was built assuming 2D plane strain (element type CPS4R/explicit), and the material far from the inspection gauge section was truncated. The truncation of the end sections would have the effect of creating a boundary that would reflect elastic waves back towards the source and onward into the gauge section. In reality, of course, this can lead to confusion of the signal, and to reduce the effect, only a short pulse of forcing is applied. Measurements taken near to the ends of the laminated beam specimen would be subject to the end reflection effect, but in practice this became an issue only towards the very end of the beam. In this analysis it was found that end sections of 60 mm in length lead to reasonable results. Investigations, by other authors [23-25], of methods to create non-reflecting boundary conditions is so far inconclusive, and the lack of a documented methodology within the latest release of the commercial package Abaqus [26] is indicative of the need for further work in this area.

The laminate ply layup was modelled explicitly, with 32 layers following a layup of $[0/90_2/0]_{4s}$; this is depicted in Fig. 7. The layers were assumed to be of equal and constant thickness of $h = 131.25 \mu\text{m}$, and with no imperfections. The material properties used in the model, defined for both the 0° and 90° plies, are given in table 1. Note that the material of the 90° plies is isotropic in the 2D plane strain analysis.

Table 1: Material properties used in the analysis model

0° plies		90° plies	
E_1	32.0 GPa	E	6.5 GPa
E_2	6.5 GPa	G	4.6 GPa
$G_{12} = G_{13}$	1.7 GPa	$\nu = E/2G - 1$	0.293
G_{23}	4.6 GPa		
ν_{12}	0.26		
Density, ρ		1835 kg m ⁻³	
Cured ply thickness, h		131.25 μ m	

Application of forcing

The experimental work suggested that for vibration excitation at a frequency of 7812.5 Hz, Lamb waves would be produced with wavelength, $\lambda_{\text{Lamb}} \approx 76$ mm. A gauge section of about 110 mm would therefore give approximately three half LAMB wavelengths. In the experimental tests, providing two sources of forcing separated by a distance of 110 was found to create an interference in the travelling LAMB waves, to give rise to a “standing wave” pattern of three half wavelengths. In the experimental work the forcing was provided by a pair of 10 mm diameter piezo-electric shaker pads, which expand and contract, to provide lateral forced displacement at the surface interface between the pads and the top layer of the beam. This lateral motion is transmitted through the material where subsequent boundary reflections, refractions and interference eventually leads to the emergence of first RAYLEIGH waves at the surface, and subsequently travelling LAMB waves.

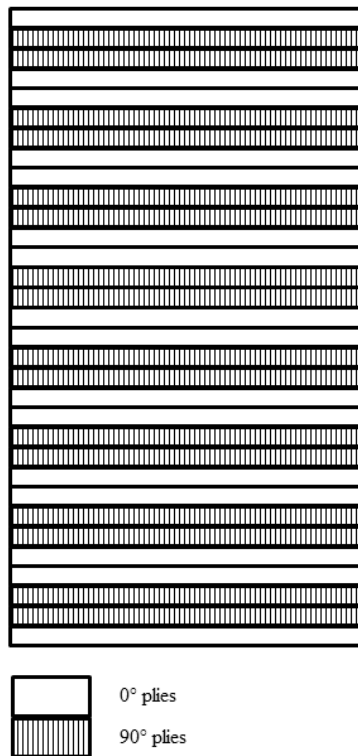


Figure 7: Laminate layup

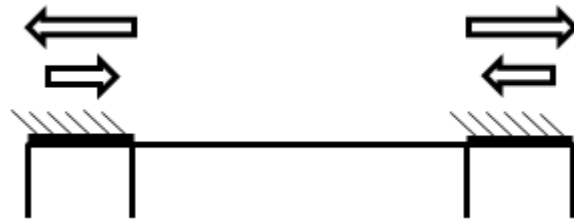


Figure 8: Load application

In the computational model, the two piezo-electric pads were represented by two plane region spanning 10 mm, over which the outer 2 mm sections moved apart and together, by an applied surface traction, Fig. 8. The inner 6 mm sections were not subjected to applied force. The forcing frequency used was $\omega = 2\pi \times 7812.5 = 49087.4 \text{ rad s}^{-1}$, and the wave form defined by $f(t) = A_0 + A_1 \cos(\omega t)$, with $A_0 = 1 \times 10^{-6}$ and $A_1 = 1$.

There were two analysis Steps defined in the model, the first had duration of $0.384 \times 10^{-3} \text{ s}$, equivalent to three periods. The second step followed on from the first, but with the forcing turned off, and ran for an additional duration of $1.28 \times 10^{-3} \text{ s}$, equivalent to a further ten periods. Unlike in the experiment, there was no windowing of the forcing function.

Meshing considerations

In order to represent the laminated nature of the specimen, it is necessary to refine the mesh sufficiently that the material property differences can be experienced by a stress wave which can be defined at the length scale of the mesh. In considering stress wave propagation note that waves propagate quicker in stiffer regions, and therefore have a longer wavelength for a given wave frequency, $c = f \lambda$. If we consider the propagation of transverse waves in the 90° plies, then this will provide us with the shortest wavelength.

Standard text books describing elastic wave propagation [27; 28] give the wave speed as

$$c_T = \sqrt{\mu/\rho} = \sqrt{G_{12}/\rho}$$

where μ is the second LAMÉ constant, and equal to the shear modulus. For the 90° plies, and for the consideration of wave propagation in the plane of the model, the appropriate shear modulus is G_{12} . In this case, $c_T = 963 \text{ m s}^{-1}$, and the corresponding wavelength at a frequency of 7812.5 Hz is $\lambda_T = 128 \text{ mm}$. To capture the detail of the waveform, the maximum element size should be no larger than a tenth of this value. In this particular example, because the forcing frequency is in kilohertz rather than megahertz range, this meshing condition is easily realized. A more detailed treatment of group velocities of waves in laminates is given by LUI and XI [29].

In explicit analysis, it is good practice to ensure that elements are of near equal size, and are approximately square. In this model, setting a global seed of 0.05 mm gave rise to three elements through the thickness of each ply (an element vertical height of $43.75 \times 10^{-3} \text{ mm}$) and horizontal length $50 \times 10^{-3} \text{ mm}$ (200 elements for every 10 mm of beam length). This leads to a model comprising of 345600 elements. For numerical stability of the explicit solution algorithm, the maximum time increment during solution must be less than the time required for a stress wave to traverse the smallest element. In this case, we should consider the fastest wave, which would be the longitudinal wave in the stiffer 0° plies. Again, from the standard texts, we have

$$c_L = \sqrt{\frac{\lambda_{\text{Lamé}} + 2\mu}{\rho}} = \sqrt{\frac{E(1-\nu)}{\rho(1+\nu)(1-2\nu)}}$$

Note that $\lambda_{\text{Lamé}}$ is the first LAMÉ constant, and should not be confused with wavelength. In the case of waves travelling in the direction of the fibers in the 0° plies, the appropriate choice for Young's modulus is E_1 , and for this case $c_L = 4619 \text{ m s}^{-1}$. The time required to traverse the element would be $\text{distance}/c_L \approx 1 \times 10^{-8} \text{ s}$. In practice, Abaqus will determine the maximum time step size automatically, but evaluating this by hand is useful in predicting analysis run time, and checking that analysis is proceeding appropriately.

It is also worth noting that for explicit finite element analysis, and other algorithms that use a central difference time marching scheme, it is usual to employ an artificial damping term. In Abaqus such terms known as “bulk viscosity factors” and are employed automatically. In the analysis describe here, the default values were taken.

Modelling of damage

In carrying out Non-Destructive Evaluation (NDE) it is important to the process of sentencing a component to know whether imperfections or damage would be benign or would propagate under subsequent loading regimes. It is therefore desirable, not only to determine the location and extent of any region of imperfection or damage, but also to have some understanding of the type of imperfection that it represents.

In the present study we consider two forms of imperfection: firstly, an imperfection that absorbs vibrational energy, and secondly, an imperfection that represents porosity or material loss. In both cases the damaged material property is applied on in one of the 10 mm regions of the gauge section of the model, in the upper four 90° plies.

1: Vibration absorbing damage

In a previous work [15], one of the present authors conducted an analytical study of the detection of damage that presented itself in the form of viscoelastic material properties. The experimental work characterized a known region of local impact crush damage by its vibration absorption characteristic at an appropriate vibration frequency. In the analysis, this material was assumed to have the same density and elastic properties as the nominal material. The phenomenology implied by such properties was artificial, but it enabled an analytical study. It further suggested that the same piezo-electric system that provided the vibration forcing could also be used to measure the total energy in the system, thereby providing an easy diagnostic process.

In a finite element analysis, there are many different energy absorbing mechanical phenomena that could be modelled. An obvious first choice would be to define a region of the model to have viscoelastic properties or to be subject to damping. Although this is seemingly simple, and enabled an analytical approach, for explicit finite element analysis this creates difficulties by significantly reducing the stable maximum time step. Given that such a model is a poor representation of reality, it would not be worth the additional computational expense.

Alternative energy absorbing phenomena, which map better onto reality include: *(i)* friction at damage interfaces, *(ii)* crack propagation, and *(iii)* plasticity. In case of impact induced resin crush damage, the concept of energy losses through friction seems compelling, but it is also rather hard to define an appropriate geometrical model for such damage interfaces, and tracking of contact surfaces in finite element is computationally expensive. In short, the computational investigation of this process is a matter for consideration in a future study. The study of crack propagation through composites has attracted a large number of researchers in recent years, although these are primarily focused on strength and life prediction of components, rather than NDE sentencing. There might be some potential to join these two goals, but a significant review of the literature is necessary, in order to avoid unintentional duplication of work.

The simplest approach is to make assumptions of “plastic-like” behavior in the crushed material: that the material in the 0° plies is relatively unaffected, since the load is carried through fibers; and that the discrete pieces comprised of fiber and crushed resin material in the 90° plies, held together by fibers which are out of the plane of the 2D analysis, can slide relatively to each other. Such motion, albeit rather granular, is not unlike the phenomenology that plasticity models describe. Plasticity has the further benefit in that it does not adversely affect the maximum time step size.

In the modelling used here, the following plasticity model data (table 2) was employed. In the analysis, the plastic strain never exceeded 0.02 strain, so the curve definition implied by the third line was never invoked.

Table 2: Plasticity data used in the analysis

	Yield ratio	Plastic strain
1	0.1	0
2	0.3	0.1
3	10	0.5

In the model, such damage was assigned to one of the 10 mm regions of the beam, to the upper 2nd, 3rd, 6th and 7th plies, Fig. 9, of the Centre Region, and Regions 5L, 4L and 3L. All other material properties were unchanged.

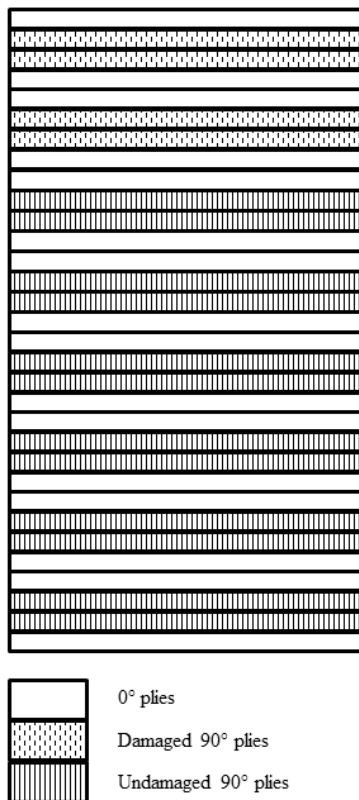


Figure 9: Damaged laminate layup

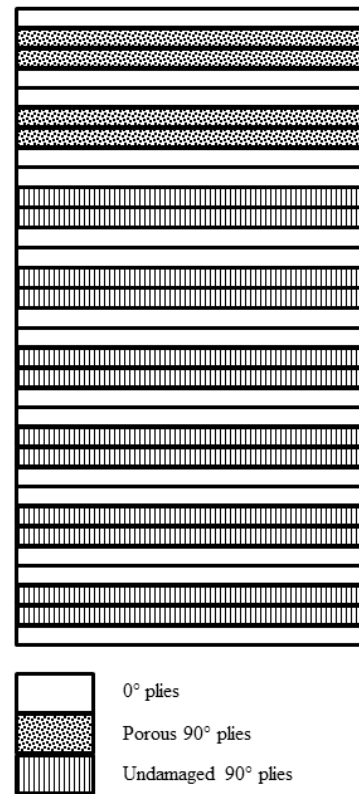


Figure 10: Laminate with porosity

2: Porosity models

The second type of imperfection considered is porosity or material loss. For simplicity, this is modelled by changing the material to have a reduced stiffness and density. As in the first form of imperfection, we reason that if a region of material is compromised through porosity

or material loss, then there is potential for vibrational energy absorption, through interfacial friction or localized damage propagation. The modified material properties therefore also included the plasticity model.

Three levels of material reduction were considered, as shown in table 3. These material models were applied to the upper 2nd, 3rd, 6th and 7th plies of Region 3L of the gauge section, as shown in Fig. 10.

Table 3: Porosity material data used in the analysis

	Pristine	90%	50%	10%
E	6.5 GPa	5.85 GPa	3.25 GPa	0.65 GPa
ρ	1835 kg m ⁻³	1651.5 kg m ⁻³	917.5 kg m ⁻³	183.5 kg m ⁻³

The justification for taking such a simplistic approach is that it is necessary to have some intuitive understanding of what might be worth further study, in which porosity and material loss are modelled as voids. At the current mesh refinement level, the material comprising a double layer of 90° plies is six elements thick: at this level of refinement, any representation of voids would be crude. As such, to take this investigation further, it would be necessary to build a highly refined local model.

4. Analysis results

Results for a pristine specimen

The analysis model was run, assuming perfect material properties, and no damage effects.

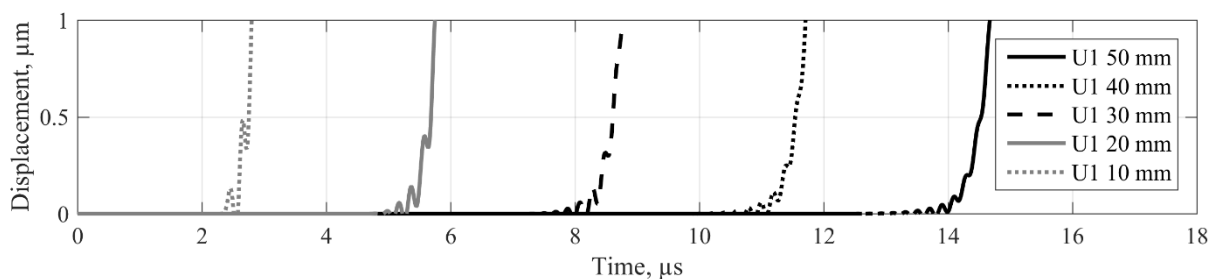


Figure 11: Displacement as a function of time, at 10 mm intervals along the gauge section.

To check that the analysis is working as expected, the initial waves generated at the shaker were tracked and the wave disturbance at distances of 10 mm, 20 mm, 30 mm, 40 mm and 50 mm from the inner edge of the shaker pad were observed. The time series displacement of at top surface nodes is shown in Fig. 11: note that it is necessary to zoom into particular time

regions of the graph to detect the initial displacement disturbances. Wave-front approximate times of arrival are shown in table 4, from which approximate wave speed can be inferred. All speeds are consistent with the predicted longitudinal wave speed in the outer ply.

Table 4: Wave-front time of arrival and approximate wave speed

Distance travelled	Time of arrival	Approximate wave speed
10 mm	2.233×10^{-6} s	4478 m s^{-1}
20 mm	4.678×10^{-6} s	4275 m s^{-1}
30 mm	7.294×10^{-6} s	4113 m s^{-1}
40 mm	10.060×10^{-6} s	3976 m s^{-1}
50 mm	12.720×10^{-6} s	3930 m s^{-1}

The development of RAYLEIGH waves is less easy to identify, as the waveguide effects of the multiple layers and the full thickness beam quickly become apparent. Within the period of time given for the first three periods of forcing, the LAMB travelling waves form and meet at the center of the beam, and the “standing wave” form is well established quite early in the subsequent non-forced analysis step.

Figure 12 shows the computed energies in the model as a function of time. Abaqus defines “ALLWK” as the total energy input into the model – this is the work done by the shaker pads. Notice that although there were only three periods of shaking, there are six peaks: these are the result of work to produce elastic strain at both the positive and negative end of the forcing amplitude. This value remains constant after time = 0.384×10^{-3} s, since this is when the forcing finished. The slight over-run just prior to that time represents a small quantity of energy given back into the shaker pads by the elasticity in the model.

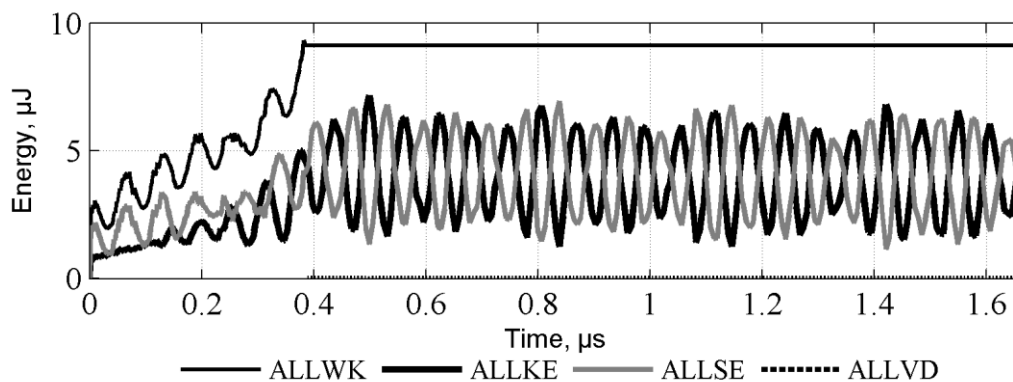


Figure 12: Computed energies in the pristine model.

“ALLKE” and “ALLSE” represent the kinetic energy and strain energy respectively. After the forcing stops, the model then experiences free vibration. Under conditions of free

vibration energy is exchanged between kinetic and strain (potential) energy, with the total energy of the system at any point in time being given by the sum of the two. The points where the ALLKE and ALLSE curves cross represent the average kinetic and strain energies, *i.e.* half of the total energy, and therefore it is to be expected that these would remain constant. The fact that there is a slight reduction is a result of numerical losses, the most significant of which is denoted by “ALLVD”, and arises from the bulk viscosity factors, which are necessary to the numerical stability of the explicit finite element central difference solver algorithm. “ETOTAL” represents the energy otherwise unaccounted for, thereby providing a means to quantify numerical error. In each case presented, the value of ETOTAL was two orders of magnitude smaller than that of ALLVD. It is therefore not plotted.

The form of the “standing wave” created by superposition of the two wave fronts is a little uneven, as the position of the nodes tends to wander. Nevertheless, the overall pattern shows approximately 3 half wave lengths within the central gauge length, and measured distances between node lines ranging between 18.8 mm and 26.4 mm. Figure 13(*i*) shows the exaggerated (scale factor = 5000×) flexural displacement reached at the end of the analysis, time = 1.664×10^{-3} s, equivalent to 13 periods at the forcing frequency. Contours indicate displacement magnitude.

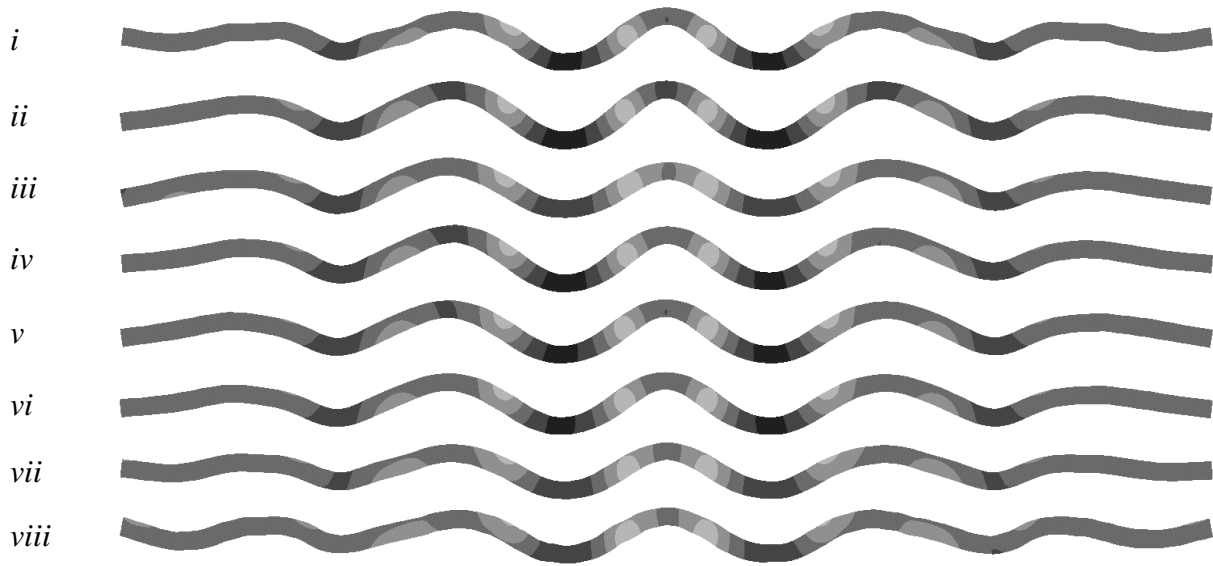


Figure 13: Exaggerated specimen flexural displacements at time = 1.664×10^{-3} s : *i* Pristine specimen, *ii* Damage in the center region, *iii* Damage in region 5L, *iv* Damage in region 4L, *v* Damage in region 3L, *vi* Porosity with 90% properties in region 3L, *vii* Porosity with 50% properties in region 3L, and *viii* Porosity with 10% properties in region 3L.

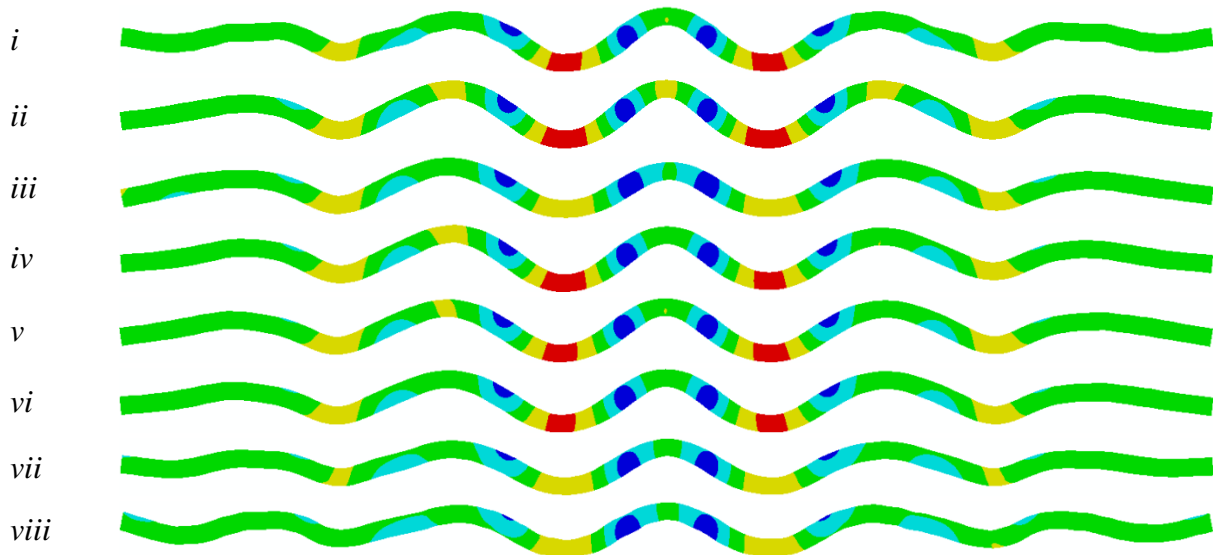


Figure 13: Exaggerated specimen flexural displacements at time = 1.664×10^{-3} s : *i* Pristine specimen, *ii* Damage in the center region, *iii* Damage in region 5L, *iv* Damage in region 4L, *v* Damage in region 3L, *vi* Porosity with 90% properties in region 3L, *vii* Porosity with 50% properties in region 3L, and *viii* Porosity with 10% properties in region 3L.

Results for energy absorbing damage at different locations

The model was modified to include the material properties representing vibration absorbing damage, in plies 2, 3, 6 and 7 of the center region and regions 5L, 4L and 3L of the gauge section. In a test situation, the shaker pads would be moved along the specimen in order to determine whether there is any damage in the gauge section. The precise location of the damage can then be pin-pointed by varying the location of the “standing wave” by adjusting the relative phase of the two shakers.

Figure 13(ii-v) shows the specimen flexural displacements for each of these cases. Notice that although in the case of damage material at regions 5L, 4L and 3L the model becomes asymmetric, there is no easily observable asymmetry in the flexural displacement. This is in agreement with an observation made by KOSTKA et al [11] that identification of the presence of damage by the effect it has on measured displacement is not feasible.

Figure 14 shows the computed energies for each of these cases. Notice that there is now an additional curve plotted for “ALLPD”: this represents the energy expended in plastic deformation.

In each of these cases, the energy expended in plastic deformation is comparable in magnitude with the kinetic and elastic energy and significantly higher than that of ALLVD. These are necessary requirements for meaningful analysis, and are a consequence of appropriate choices of the plasticity parameters given in table 3.

Notice that the plastic deformation energy differs in each case, and in particular, that the lowest plastic deformation energy is observed for the case of damage material at the center region. In order to understand this, consider the locations of the nodes of the “standing wave”. For a sinusoidal “standing wave” of wave length equal to two thirds of the gauge section, the node lines would divide the gauge section into precisely three equal lengths, at positions 36.7 mm and 73.3 mm as measured from the left hand edge. These positions correspond with the location of regions 4L and 4R. From the model flexural displacement results it is clear that a true “standing wave” was not created, and the observed node positions wandered. Half wave lengths of between 18 mm and 26 mm place the nodes between around 42 mm and 46 mm, and between around 64 mm and 68 mm, in regions 5L and 5R.

Levels of plastic strain are shown in Fig. 15. The elements are rather small, so rather than show the element boundaries explicitly and obscure the plastic strain values, a “quilt” plot has been used. Each element is assigned a single value, and mesh size can be inferred from the steps in grey-scale change. Notice how it is the lower plies, plies 6 and 7, which experience the highest levels of plastic strain. The greatest total plastic strain occurs when the damage material is in region 5L, centered at a position at approximately 44.5 mm from the left hand edge of the gauge section.

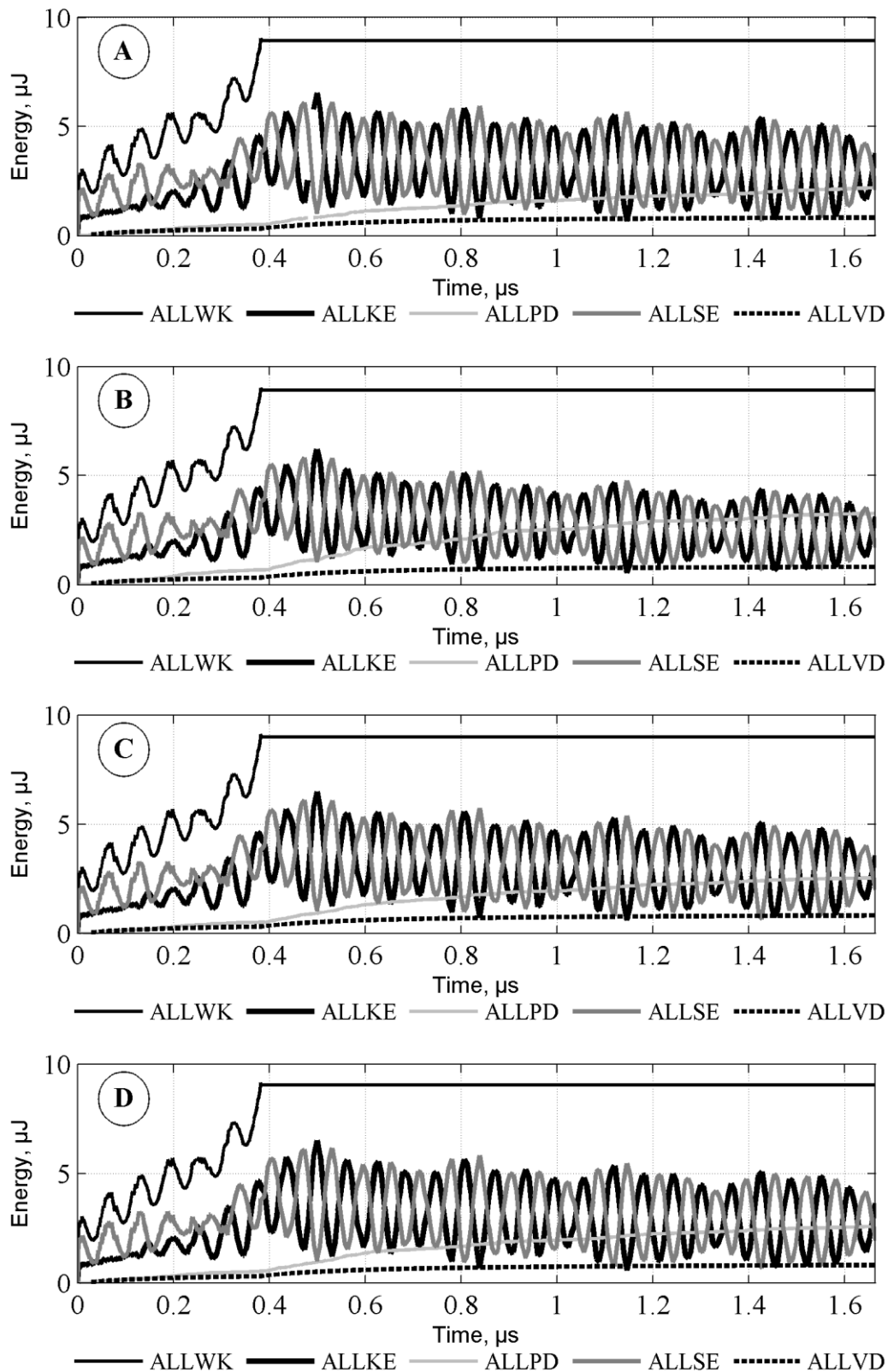



Figure 14: Computed energies in the models with energy absorbing damage. (A) For damaged material in the center region. (B) For damaged material in the 5L region. (C) For damaged material in the 4L region. (D) For damaged material in the 3L region.

A small amount of hour-glassing was observed in the elements near the corners of each region. Hour-glassing is impossible to completely avoid, but arising energy losses have been monitored and remain insignificant compared with the data presented.



Figure 15: Plastic strain distributions in the damage regions

Range 0 – 1.4% strain, PEEK value scale light to dark in 0.2% steps 

i – Center Region, *ii* Region 5L, *iii* – Region 4L, *iv* – Region 3L.

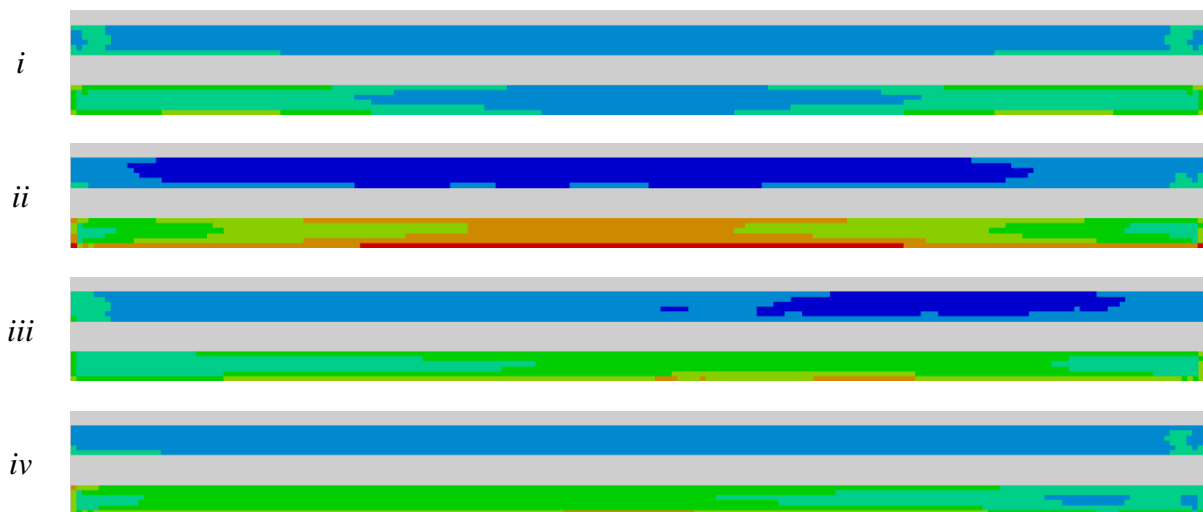



Figure 15: Plastic strain distributions in the damage regions

Range 0 – 1.4% strain, PEEK value scale blue to red in 0.2% steps 

i – Center Region, *ii* Region 5L, *iii* – Region 4L, *iv* – Region 3L.

Results for differing levels of porosity or material loss

In the final computational analyses of this study, the effect of porosity or material loss, coupled with energy absorbing damage is investigated. In this case, region 3L was selected

to be the site for the material with the modified properties. Results are presented in Figs 13(vi, vii, viii), 16 and 17.

In the cases of material that retains 90% or 50% of its properties, the energy losses shown in Fig. 16 are comparable with energy loss shown in Fig. 14 region 3L, for the material with only energy absorbing damage. In the case of material which retains only 10% of stiffness and density, the energy loss drops below the numerical damping energy. Figure 17 echoes this showing low values for plastic strain. This is an important observation: regions of porosity or material loss off-load their load carrying duty to neighboring regions. The stresses in the neighboring regions are therefore slightly increased, but for localized porosity or damage the change in stresses in the neighborhood are small. The accompanying loss of local density has the effect of reducing dynamic loading. Thus the low density and low stiffness region carries relatively little load and creates relatively little dynamic load, resulting in relatively low strains within the region. As a result, a component suffering localized damage exhibiting high porosity or material loss will not necessarily show a positive result when assessed for energy absorbing damage.

5. Conclusions

Experimental tests, making use of wave superposition from two shaker sources, have been able to generate interference between LAMB waves which leads to a wave form resembling a “standing wave” at the center of a gauge section. The same piezo-electric system which provided the source of vibration can also be used to measure the elastic energy remaining in the specimen. This has been found to be a viable methodology for detection of energy absorbing damage on the specimen, such as might be created by impact or crush loads.

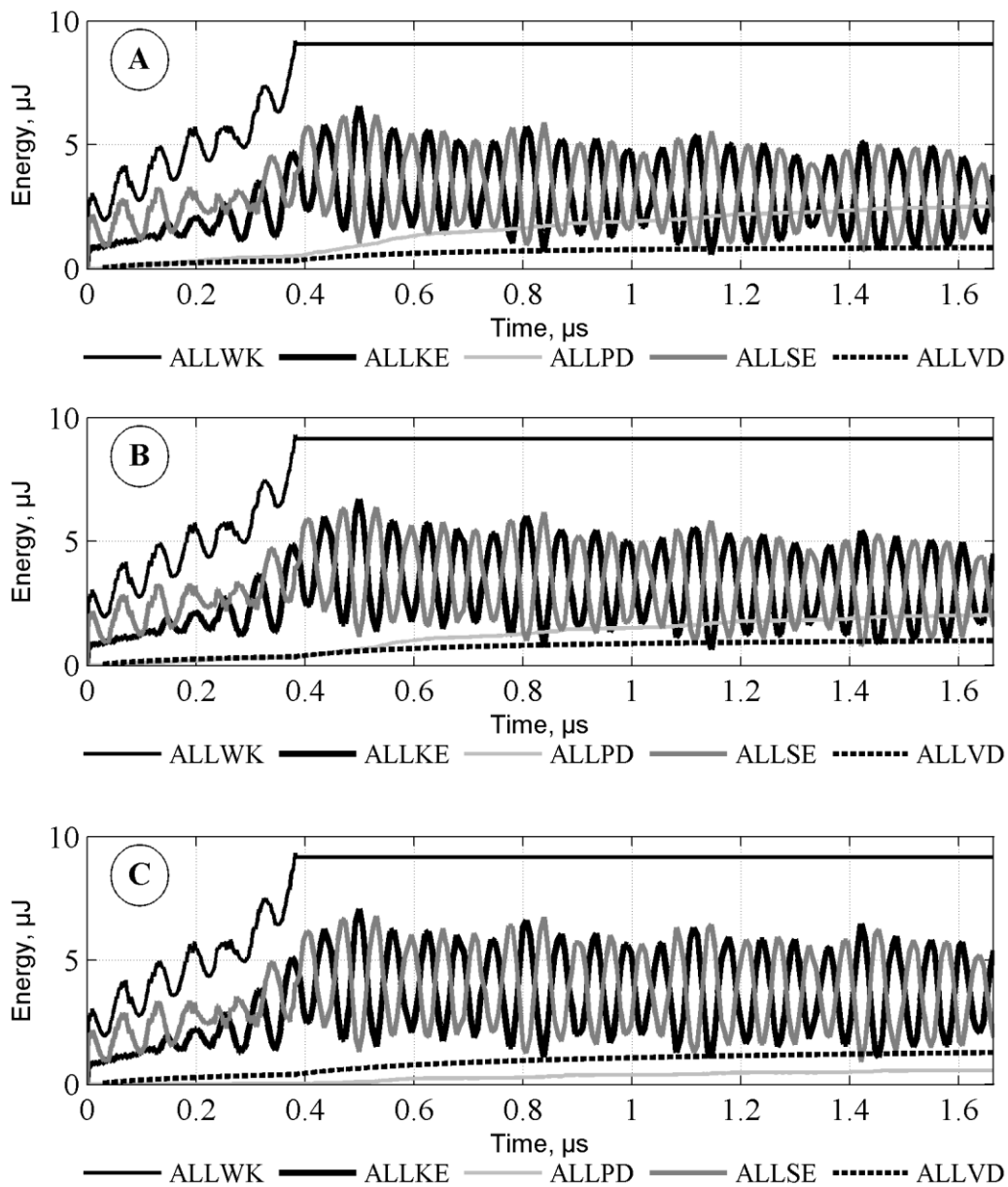


Figure 16: Computed energies in the models with porosity or material loss. **(A)** For material that retains 90% of its properties. **(B)** For material that retains 50% of its properties. **(C)** For material that retains 10% of its properties.


The potential for such a methodology for accurate damage location identification, and for sentencing type of damage is clearly of interest. Computational analysis to investigate this was performed, using simple material model variations to determine what might be the critical issues.

The computational analysis was able to replicate the LAMB wave generation and produced a wave form resembling a “standing wave”. The anticipated LAMB wave length was around

73 mm, while the wave length obtained through the computation was around 45 mm. Although not an ideal correlation, the result is encouraging, and further work including 3D analysis and longer end sections might lead to better understanding.




Figure 17: Plastic strain distributions in the porosity damage regions

Range 0 – 1.4% strain, PEEK value scale light to dark in 0.2% steps 

i – 90% properties, *ii* – 50% properties, *iii* – 10% properties.



Figure 17: Plastic strain distributions in the porosity damage regions

Range 0 – 1.4% strain, PEEK value scale blue to red in 0.2% steps 

i – 90% properties, *ii* – 50% properties, *iii* – 10% properties.

The precise ratio of the length of the gauge section and the LAMB wavelength does not seem to be critical, although the location of the “standing wave” node relative to the location of the damage is significant in the measurement of energy loss from the system. The wandering of the node position is a feature of not achieving an exact half wavelength ratio, and it is to be expected that for the detection and measurement of small regions of damage it will be necessary to minimize the wander.

Detection of regions which exhibit some porosity or material loss will also be feasible using this method, but in cases where the material loss is significant, it is to be expected that the technique will be prone to giving a false negative result.

Further work is desirable, in developing higher fidelity models of material which show the damage morphology explicitly. Examples should include crack surface to surface friction and micro-crack propagation. Examples modelling porosity voids, delamination, and surface damage where material is removed, should also be modelled.

Acknowledgements

The authors wish to acknowledge Glyndwr University and the Technische Universität Dresden for on-going support and access to facilities.

References

- [1] Ashby, M.F., *Materials selection in mechanical design*, Butterworth-Heinemann Amsterdam, Boston, 2005.
- [2] Cantwell, W.J. and Morton, J., “The impact resistance of composite materials — a review,” *Composites*, Vol. 22, No. 5, 1991, pp. 347–362.
- [3] Yang, F.J. and Cantwell, W.J., “Impact damage initiation in composite materials,” *Composites Science and Technology*, Vol. 70, No. 2, 2010, pp. 336–342.
- [4] Kostka, P., Holeczek, K. and Hufenbach, W., *Characterisation of impact-caused changes of the anisotropic material damping of composite laminates* Venice, Italy.
- [5] McMillan, A.J., Monroy, Aceves C., and Sutcliffe, M.P.F., “Moderate energy impact analysis combining phenomenological contact law with localized damage and integral equation method,” *Int. J. Impact Engng.*, Vol. 43, 2012, pp. 29-39, DOI: 10.1016/j.ijimpeng.2011.11.008
- [6] Nicolais, L., Meo, M. and Milella, E., *Composite materials: A vision for the future*, Springer London, 2011.
- [7] Farrar, C.R. and Lieven, N., “Damage prognosis: the future of structural health monitoring,” *Philosophical Transactions of the Royal Society A: Mathematical, Physical and Engineering Sciences*, Vol. 365, No. 1851, 2007, pp. 623–632.
- [8] Hao, S., Strom, B.W., Gordon, G., Krishnaswamy, S. and Achenbach, J.D., “Scattering of the Lowest Lamb Wave Modes by a Corrosion Pit,” *Research in Nondestructive Evaluation*, Vol. 22, No. 4, 2011, pp. 208–230.
- [9] McMillan, A.J., “Geometry generation challenges for modelling and analysis of micro-structured materials,” *Journal of Physics Conference Series: Materials Science and Engineering*, (Advanced Materials for Demanding Applications, St Asaph, 7-9 April 2014), Vol. 74, 2015, DOI: 10.1088/1757-899X/74/1/012010

- [10] McMillan, A.J., “Defect identification and characterization algorithms for assessing effect on component strength,” Proceedings 15th European Conference on Composite Materials, Venice, 24-28 June, 2012.
- [11] McMillan, A.J., Archer, E., McIlhagger, A., Lelong, G., “Strength knock-down assessment of porosity in composites: modelling, characterizing and specimen manufacture,” *Journal of Physics Conference Series: (Modern Practice in Stress and Vibration Analysis, Glasgow, 29-31 August 2012)*, Vol. 382, 2012, DOI: 10.1088/1742-6596/382/1/012027
- [12] McMillan, A.J., “Material strength knock-down resulting from multiple randomly positioned voids,” *J Reinforced Plastics & Composites*, Vol. 31(1), 2012, pp. 13-28, DOI: 10.1177/0731684411422614
- [13] Montalvao, D., “A Review of Vibration-based Structural Health Monitoring with Special Emphasis on Composite Materials,” *The Shock and Vibration Digest*, Vol. 38, No. 4, 2006, pp. 295–324.
- [14] Kostka, P., Holeczek, K., Filippatos, A., Langkamp, A. and Hufenbach, W., “In situ integrity assessment of a smart structure based on the local material damping,” *Journal of Intelligent Material Systems and Structures*, Vol. 24, No. 3, 2013, pp. 299–309.
- [15] Smith, C.B. and Wereley, N.M., “Transient analysis for damping identification in rotating composite beams with integral damping layers,” *Smart Materials and Structures*, Vol. 5, No. 5, pp. 540.
- [16] Kostka, P., Holeczek, K. and Hufenbach, W., “A new methodology for the determination of material damping distribution based on tuning the interference of solid waves,” *Engineering Structures*, Vol. 83, 2015, pp. 1–6.
- [17] McMillan, A.J. “Computational modeling of ultrasound propagation using Abaqus explicit,” Proceedings of the Simulia UK Regional Users Meeting, Crewe 18-19 September 2013.
- [18] Kostka, P., Holeczek, K., Hufenbach, W. and Langkamp, A., *Verfahren zur Identifikation lokaler Werkstoffdämpfung in Verbund-Strukturen*, No. EP 2 696 184 A2, 2014.
- [19] Holeczek, K., Kostka, P. and Modler, N., “Dry Friction Contribution to Damage-Caused Increase of Damping in Fiber-Reinforced Polymer-Based Composites,” *Advanced Engineering Materials*, Vol. 16, No. 10, 2014, pp. 1284–1292.
- [20] Riande, E., Diaz-Calleja, R., Prolongo, M., Masegosa, R. and Salom, C., *Polymer Viscoelasticity: Stress and Strain in Practice*, Taylor & Francis, 1999, pp. 243.

- [21] Bhalla, S. and Kiong Soh, C., “Structural impedance based damage diagnosis by piezo-transducers,” *Earthquake Engineering & Structural Dynamics*, Vol. 32, No. 12, 2003, pp. 1897–1916.
- [22] Su, Z. and Ye, L., *Identification of damage using Lamb waves: from fundamentals to applications*, Springer Science & Business Media, 2009, pp. 69.
- [23] Hosseini, S.M., Duczek, S. and Gabbert, U., “Non-reflecting boundary condition for Lamb wave propagation problems in honeycomb and CFRP plates using dashpot elements,” *Composites Part B: Engineering*, Vol. 54, 2013, pp. 1–10.
- [24] Drozd M.B., *Efficient finite element modelling of ultrasound waves in elastic media*, PhD Thesis, University of London, 2008.
- [25] Jahanbin, M., private communication.
- [26] Dassault Systèmes Simulia Corp., “ABAQUS/Standard user manual, version 6.14, 2014.
- [27] Achenbach, J., *Wave propagation in elastic solids*, Elsevier, Amsterdam, 2012, pp. 122.
- [28] Kolsky, H., *Stress waves in solids*, Dover Publications, New York, 1963, pp. 13.
- [29] Liu, G.R. and Xi, Z.C., *Elastics waves in anisotropic laminates*, CRC Press, Boca Raton, 2002, pp. 43.